Decoupling the Roles of Carbon and Metal Oxides on the Electrocatalytic Reduction of Oxygen on La1-xSrxCoO3-δ Perovskite Composite Electrodes

Journal:	*Physical Chemistry Chemical Physics*
Manuscript ID	CP-ART-10-2018-006268.R1
Article Type:	Paper
Date Submitted by the Author:	11-Dec-2018
Complete List of Authors:	Mefford, J.; The University of Texas at Austin, Department of Chemistry; The University of Texas at Austin, Center for Nano and Molecular Science and Technology; Department of Materials Science and Engineering, Stanford University, Stanford, California, 94305, USA Kurilovich, Aleksandr; Skolkovo Institute of Science and Technology, Center for Electrochemical Energy Storage CREI Saunders, Jennette; The University of Texas at Austin, Department of Chemistry Hardin, William; The University of Texas at Austin, Texas Materials Institute; The University of Texas at Austin, Center for Nano and Molecular Science and Technology; Exponent Failure Analysis Associates Abakumov, Artem; Skolkovo Institute of Science and Technology, Center for Electrochemical Energy Storage CREI; EMAT, University of Antwerp, Groenenborgerlaan 171, B-2020 Antwerp, Belgium Forslund, Robin; The University of Texas at Austin, Department of Chemistry, Bonnefont, Antoine; Université de Strasbourg, Insititut de Chimie de Strasbourg Dai, Sheng; Oak Ridge National Laboratory, Johnston, Keith; University of Texas at Austin, Department of Chemical Engineering; The University of Texas at Austin, Texas Materials Institute Stevenson, Keith; Skolkovo Institute of Science and Technology, Center for Electrochemical Energy Storage CREI

Physical Chemistry Chemical Physics

ARTICLE

Decoupling the Roles of Carbon and Metal Oxides on the Electrocatalytic Reduction of Oxygen on $La_{1-x}Sr_xCoO_{3-\delta}$ Perovskite Composite Electrodes

Received 00th January 20xx,
Accepted 00th January 20xx

DOI: 10.1039/x0xx00000x

www.rsc.org/

J. Tyler Mefford,[a,b,*] Aleksandr Kurilovich,[c] Jennette Saunders,[a] William G. Hardin,[b,d,§] Artem M. Abakumov,[c,e] Robin P. Forslund,[a,b] Antoine Bonnefont,[f] Sheng Dai,[g] Keith P. Johnston,[d,h] Keith J. Stevenson[c,†]

Perovskite oxides are active room-temperature bifunctional oxygen electrocatalysts in alkaline media, capable of performing the oxygen reduction reaction (ORR) and oxygen evolution reaction (OER) with lower combined overpotentials relative to their precious metal counterparts. However, their semiconducting nature necessitates the use of activated carbons as conductive supports to generate applicably relevant current densities. In efforts to advance the performance and theory of oxide electrocatalysts, the chemical and physical properties of the oxide material often takes precedence over contributions from the conductive additive. In this work, we find that carbon plays an important synergistic role in improving the performance of $La_{1-x}Sr_xCoO_{3-\delta}$ ($0 \le x \le 1$) electrocatalysts through the activation of O_2 and spillover of radical oxygen intermediates, HO_2^- and O_2^-, which is further reduced through chemical decomposition of HO_2^- on the perovskite surface. Through a combination of thin-film rotating disk electrochemical characterization of the hydrogen peroxide intermediate reactions (hydrogen peroxide reduction reaction (HPRR), hydrogen peroxide oxidation reaction (HPOR)) and oxygen reduction reaction (ORR), surface chemical analysis, HR-TEM, and microkinetic modeling on $La_{1-x}Sr_xCoO_{3-\delta}$ ($0 \le x \le 1$)/carbon (with nitrogen and non-nitrogen doped carbons) composite electrocatalysts, we deconvolute the mechanistic aspects and contributions to reactivity of the oxide and carbon support.

Introduction

In the ongoing efforts to develop renewable energy systems, regenerative alkaline fuel cells and rechargeable metal-air batteries have been identified as attractive energy storage and conversion devices with energy densities similar to fossil fuels. Crucial to the success of these technologies is the identification of effective bifunctional air electrodes that are active for both charging the cells (oxygen evolution reaction, OER, $4OH^- \rightarrow O_2 + 2H_2O + 4e^-$) and discharging (oxygen reduction reaction, ORR, $O_2 + 2H_2O + 4e^- \rightarrow 4OH^-$)—both of which require catalysts due to their sluggish reaction kinetics that result in large overpotentials for both reactions, thereby reducing the efficiency of the systems.[1–4] Commercial catalysts for these reactions rely on Pt group metals, limiting the availability of fuel cells and metal air batteries in consumer applications.[5–7] In response to this, metal oxides have been identified as viable alternatives due to the high activities they have shown for both reactions, their stability in alkaline conditions, and the significant decrease in cost associated with their use. While a number of mechanistic schemes have been put forward to explain the reactivity of metal oxides for the OER/ORR, the complexity of the reactions, which involve 4 electron and 4 proton transfers, as well as possible additional coupled chemical reaction steps under different electrochemical conditions have not yielded conclusive results that enable the rational design of active catalysts. Of the metal oxide systems, perovskites, with the general formula $A'_{1-x}A''_xB'_{1-y}B''_yO_{3\pm\delta}$, where A' and A'' are large alkali-earth or rare-earth elements and B' and B'' are transition metals, are an appealing model system because the physicochemical and electronic properties of these materials can be easily tuned through substitution into the A and B sites, as well as through the formation of oxygen vacancies, δ.[8,9] However, the large size of the perovskite

[a] Department of Chemistry, The University of Texas at Austin, Austin, TX 78712, USA
[b] Center for Nano and Molecular Science and Technology, The University of Texas at Austin, Austin, TX 78712, USA
[c] Center for Electrochemical Energy Storage CREI, Skolkovo Institute of Science and Technology, 143025 Moscow, Russia
[d] Texas Materials Institute, The University of Texas at Austin, Austin, TX 78712, USA
[e] Electron Microscopy for Materials Science EMAT, University of Antwerp, B-2020 Antwerp, Belgium
[f] Institut de Chimie de Strasbourg, University of Strasbourg, 67070 Strasbourg, France
[g] Chemical Sciences Division, Oak Ridge National Laboratory, Oak Ridge, TN 37831, USA
[h] Department of Chemical Engineering, The University of Texas at Austin, Austin, TX 78712, USA
*Present Address: Department of Material Science and Engineering, Stanford University, Stanford, CA 94305, USA
§ Present Address: Exponent Failure Analysis Associates, Natick, MA 01760, USA

† Correspondence and requests for materials should be addressed to K.J.S. (email: k.stevenson@skoltech.ru)

Electronic Supplementary Information (ESI) available: See DOI: 10.1039/x0xx00000x

particles coupled with their relatively low electrical conductivities necessitate the use of a conductive support, generally manifested through mixing the perovskites with high-surface area carbons. The use of carbon in these composite systems adds additional levels of complexity to studying ORR and OER catalysis on these systems which for the most part have been largely underestimated in the published works on the topic.[10–12] Historically it is well documented that carbon is an active catalyst in alkaline electrolytes for the two electron reduction of oxygen to peroxide.[13–15] In this vein, the complicated synergistic role of carbon in the ORR has developed, whereby reaction intermediates produced on the carbon may spillover onto the oxide and further react in order to achieve the full 4 e^- ORR on composite electrodes.[16–24] As such, the development of active
bifunctional electrodes necessitates both the optimization of the oxide catalysts as well as the carbon supports. Thus the aim of this paper is to elucidate the individual contributions of the carbon support and the perovskite oxide series $La_{1-x}Sr_xCoO_{3-\delta}$ in the ORR in order to decouple what controls the rate limiting steps (i.e. kinetics) and overall ORR mechanistic pathway in the carbon supported perovskite composite systems.

Physical and Surface Properties of $La_{1-x}Sr_xCoO_{3-\delta}$

The physical properties of a series of Sr substituted lanthanum cobalt oxides, $La_{1-x}Sr_xCoO_{3-\delta}$, where, for instance LSCO28 refers to $La_{0.2}Sr_{0.8}CoO_{3-\delta}$, have been described in a previous publication.[25] In this work, we develop an increased understanding of the surface properties of the series through O1s X-ray photoelectron spectroscopy (XPS) and HAADF and ABF-STEM imaging with atomic resolution EDX. Using our general synthetic protocol of reverse-phase hydrolysis of metal nitrate salts followed by thin-film freezing and lyophilization, the whole series from $0 \le x \le 1$ was synthesized as perovskite phase nanocrystals as measured by powder X-ray diffraction and transmission electron microscopy, including the previously unreported oxygen-vacancy-ordered perovskite phase $SrCoO_{2.7}$, which differs from the face-sharing hexagonal prismatic phase $Sr_6Co_5O_{15}$ and from the highly oxygen-deficient brownmillerite phase $SrCoO_{2.5}$ (see Supporting Information for synthesis details).[26–28] The synthesis yields catalysts with morphologies of sintered primary nanoparticles of ~50 – 100 nm, forming agglomerates with average diameter of ~300nm – 1 µm. BET surface areas were relatively consistent across the entire series, ranging from 3.1 to 4.5 $m^2\ g^{-1}$.[25]

Table 1: Cobalt oxidation state, oxygen vacancy concentration, and surface hydroxylation versus Sr substitution for La1-xSrxCoO3-δ

x	Cobalt Oxidation State	Vacancy Stoichiometry, δ	XPS Surface Hydroxylation
0	3.01 ± 0.01	-0.01 ± 0.01	7.1%
0.2	3.18 ± 0.02	0.01 ± 0.01	31%
0.4	3.30 ± 0.08	0.05 ± 0.04	34%
0.6	3.43 ± 0.01	0.09 ± 0.01	38%
0.8	3.48 ± 0.01	0.16 ± 0.01	59%
1.0	3.40 ± 0.06	0.30 ± 0.03	63%

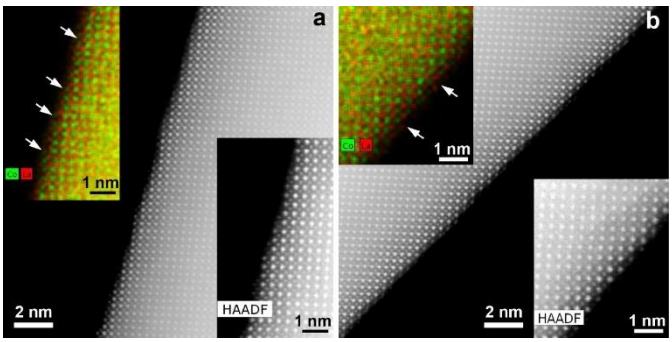

Figure 1: HAADF-STEM images and atomic resolution EDX compositional maps of the curved surfaces of $LaCoO_3$ particles viewed along $<001>_p$. (**a**) The surface consisting of the (LaO)-terminated $\{100\}_p$ terraces stepped by one perovskite unit cell. (**b**) The surface consisting of the (LaCoO)-terminated $\{110\}_p$ terraces with the steps of one layer width. The inserts show enlarged HAADF-STEM images of the regions used for the EDX mapping and the color-coded mixed Co and La compositional maps (Co – green, La – red). The steps between the terraces are marked with arrows.

Chemical titration measurements of the oxygen stoichiometry across the series show a trend of increasing oxygen deficiency and increasing
cobalt oxidation state with increasing Sr^{2+} substitution for La^{3+}. In addition, it was shown through XPS that surface hydroxylation increases substantially with Sr substitution, partially as a function of cobalt oxidation state, and from the presence of surface oxygen vacancies which act as dissociation sites for water (analysis is provided in the Supporting Information and Figure S1). These results are presented in Table 1.

To gain further insight into the structure of the LSCO perovskite surfaces, high angle annular dark field (HAADF) and annular bright field (ABF) scanning transmission electron microscopy and atomic resolution energy dispersive X-ray (EDX) spectroscopy were performed on LSCO particles. Although theoretical considerations of the electrocatalysis on perovskites have suggested that the $\{100\}_P$ plane is the active surface due to the high density of exposed B-site atoms,[12,29–32] the actual surface structure of the LSCO particles appears to be significantly different. Bright field transmission electron microscopy image of $LaCoO_3$, as a representative case, shows that the particles are round-shaped reflecting that the low index $\{100\}_p$, $\{110\}_p$ or $\{111\}_p$ perovskite planes are not dominating and curved surface should possess more complex structure (Supporting Figure S2). **Figure 1** shows the fragments of the curved surfaces of $LaCoO_3$ viewed along the $<001>_p$ pseudocubic axis. They demonstrate clearly pronounced stepped (vicinal) structure. The surface in Figure 1a is composed of short fragments (~1-2 nm) of peroskite $\{100\}_P$ layers separated by steps of one perovskite unit cell in the direction across the layers. At these terraces the perovskite structure is terminated by the (LaO) perovskite layer, leaving the (CoO_2)

layers beneath, so that the transition metal sites become sterically available only at the steps terminating the facets. The <001>$_P$ view at vicinal surface formed by the ~2 – 3 nm {110}$_P$ fragments shows that the terraces are terminated with the (LaCoO) layers making the Co cations directly accessible (Figure 1b). The {110}$_P$ terraces are separated by steps with a thickness of one (LaCoO) layer.

Besides more or less regular curved surfaces with the terraces of the same crystallographic orientation and nearly the same length, the irregular curved surfaces can be also found, consisting of the segments with variable lengths and crystallographic orientation (Supporting Figure S3a). Such surfaces may arise from cleaving along the incoherent grain boundaries between the nanocrystals (Supporting Figure S3b), and demonstrate the complexity in modeling catalysis on perovskite systems. Although the low-index facets are not the most abundant components of the surface of the $LaCoO_3$ particles, the extended segments of the {100}$_P$ and {110}$_P$ surfaces without the stepped terraces were also observed. The terminating layer at the {100}$_P$ surface viewed along <001>$_P$ shows noticeable reconstruction, where the last (CoO_2) layer of the perovskite structure is topped with an extra Co-rich layer, forming a staggered arrangement of the transition metal columns (Supporting Figure S4). The {110}$_P$ surface viewed along <1 1 0>$_P$ reveals the (LaCoO) termination without noticeable surface reconstruction (Supporting Figure S5).

Our preliminary observations on the LSCO82, LSCO28 and SCO particles revealed that the vicinal surface structure is also dominating in these samples, although the regularity of the surface steps generally decreases with increasing the Sr content. The detailed analysis of the surfaces in these samples requires mapping of the La/Sr distribution, Co oxidation state and, possibly, oxygen vacancies being beyond the scope of the present article.

Oxygen and Peroxide Electrocatalysis on $La_{1-x}Sr_xCoO_{3-\delta}$/Carbon Composites

The electrocatalytic activity of the LSCO series for the ORR was measured through thin-film rotating disk electrochemistry in O_2 saturated 0.1 M KOH at a rotation rate of 1600 RPM and a scan rate of 5 mV s^{-1}. In order to decouple the activities of the LSCO members from the contributions of the carbon to the ORR, the perovskite catalysts were supported at 30 wt% on two different carbons, Vulcan carbon XC-72 (VC) and a 2 at. % nitrogen-doped mesoporous carbon (NC) (full experimental details are provided in the Supporting Information). SEM images of the composite electrodes are included in Figures S6 and S7 of the Supporting Information. In general, although the morphology of the VC and NC are different, with ~100 nm spherical particles for VC and ~300-500 nm flake shaped mesoporous particles for the NC, both carbons form similar conformal coatings of the perovskite particles. Mass-normalized Tafel plots of the polarization curves are presented in **Figure 2**. Each member of the series shows similar Tafel slopes at given potentials on the respective carbons, indicating

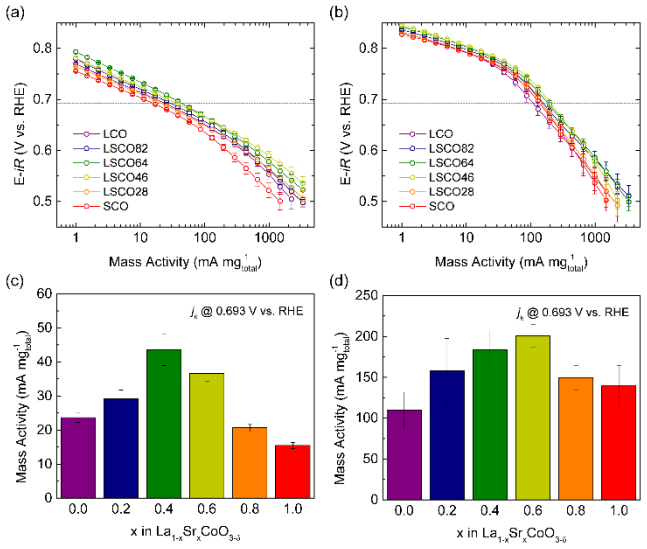

Figure 2. Tafel plots of 30 wt% LSCO perovskite composite electrocatalysts supported on a) Vulcan carbon and on b) nitrogen-doped mesoporous carbon at a scan rate of 5 mV s^{-1} and rotation rate of 1600 rpm in the negative potential direction in O_2 saturated 0.1 M KOH. Mass activities (kinetic current densities) at 0.693V vs. RHE for LSCO perovskite catalysts on c) Vulcan carbon and on d) nitrogen-doped mesoporous carbon. All activities have been mass transport-corrected, *iR* corrected, and normalized to the total electrode mass loading of 51 µg cm^{-2}_{geom}. Error bars represent standard deviations of 5 replicate measurements.

that the same intermediate reaction is rate-limiting for all members of the LSCO series regardless of the degree of Sr substitution. Evident also is the influence of carbon in the ORR on the composite systems. On VC, the Tafel slopes remains relatively constant across the kinetic region of potentials, with a slope of ~59 mV dec^{-1} (2.303*RT/F) indicative of moderate coverage of the rate-limiting intermediate and increasing only slightly at more cathodic potentials. On NC, the current response shows two different kinetic regions. At the low overpotential region (0.85 to 0.75 V vs. RHE) it shows increased kinetics as compared to VC with Tafel slopes of ~40 mV dec^{-1} (2RT/3F), but at high overpotentials (E < 0.75 V vs. RHE) the slope triples to ~120 mV dec^{-1} (2.303*2RT/F) suggesting that the reaction moves into a potential regime of high intermediate coverage on the catalyst surface. Similar to the results of Li et al., an analysis of the onset potential, defined in this study as 25 µA cm^{-2}_{geom}, shows an ~100 mV positive shift for the catalysts when switching from VC to NC (Supporting Figure S8).[33] This shift is also apparent in the current-potential curves for the pure carbons without LSCO catalysts, and leads to an approximately five-fold increase in activity for the composite systems. We speculate that the increased onset potential on NC is due to a combination of increased active edge and defect sites as well as an increased electron density at the Fermi level due to the incorporation of nitrogen.[4,34,35] This increased density should allow for an increased propensity for the first electron transfer to O_2 and higher activity for the production of HO_2^- as has been previously proposed by our group.[36,37]

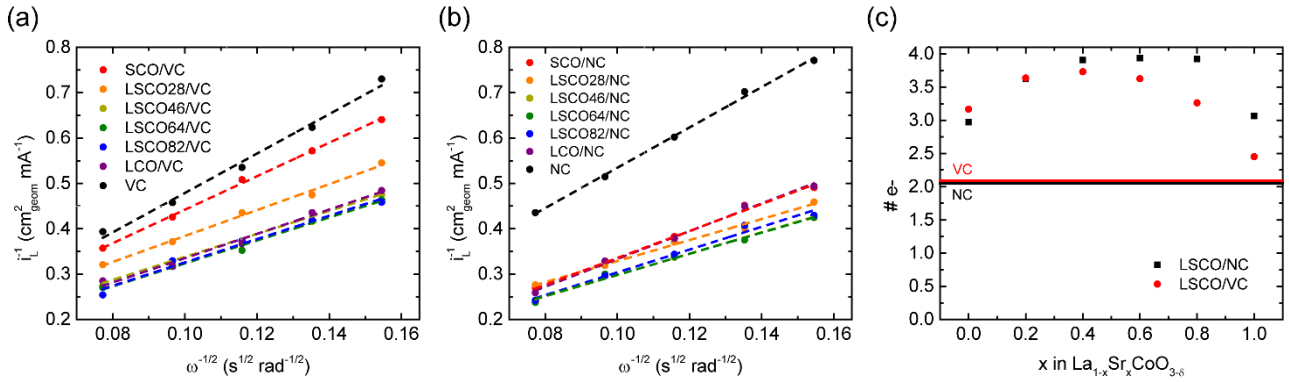

Figure 3. Koutecky-Levich analysis of LSCO perovskite composite electrocatalysts supported on (**a**) Vulcan carbon and on (**b**) nitrogen-doped mesoporous carbon at the limiting current potential of 0.4V vs. RHE. (**c**) Total number of electrons transferred during the ORR derived from the slope of the Koutecky-Levich plots. The number of electrons transferred on each of the carbons without LSCO are marked as lines on the graph.

In contrast to the OER, the observed activities for the ORR on LSCO did not trend with the vacancy concentration, δ, which increases with Sr substitution, x. Neither do these results fit on the volcano plot for e_g filling as proposed by Suntivich.[12] Instead, the trend in activities supports the band theory hypothesis proposed by Matsumoto in which the σ* band formed between the metal d_z2 orbital and the oxygen adsorbate O sp_σ orbital, which controls that charge transfer characteristics and adsorption strength of intermediates, which can be optimized through tuning the electronic energy of the Co active site to achieve maximum overlap of the orbitals.[31,32,38–41] The difference in activity trends between the OER and ORR for the series suggests a differing rate-limiting step and corresponding adsorbate energy. In this study, the cobalt oxidation state is directly tuned through the degree of Sr substitution as demonstrated in Table 1. For the LSCO series supported on both carbons, the activity increases towards the middle compositions (LSCO64 and LSCO46). It is interesting to note that on VC LSCO64 is the most active catalyst but on NC, the maximum activity shifts to LSCO46. Due to the increased Sr substitution, the bulk oxidation state of cobalt is higher in LSCO46 than in LSCO64. Although the surface oxidation state of cobalt is expected to be similar for all members of the LSCO series during the rate-limiting step, the absolute energy position of the $Co^{3+/4+}$ surface redox couple should trend with the position of the M-3*d*/O-2*p* σ* band in the bulk, which is modulated through the oxidation state of cobalt and La:Sr stoichiometry and shifts towards the oxide O 2*p* band with increasing Sr content. The shift in activities for LSCO on the different carbons suggests a differing degree of electron density donation from the different carbons due to the formation of a p-n junction at the interface between the p-type semiconducting LSCO particles and the n-type N-doped carbon, which further modulates the surface $Co^{3+/4+}$ redox position (surface Fermi level) in LSCO around the redox couple of the intermediate species. Although not measured in this study, this shift of electron energy to the transition metal active sites have been observed through XAS in a number of perovskites and other metal oxide electrocatalysts coupled with carbon supports.[42–44] It should be noted that amongst the series, the most active compositions of LSCO64/VC and LSCO46/NC were about twice as active as the least active compositions supported on their respective carbons (44 ± 5 mA mg^{-1}_{total} for LSCO64/VC versus 15.5 ± 0.9 mA mg^{-1}_{total} for SCO/VC; 200 ± 14 mA mg^{-1}_{total} for LSCO46/NC versus 110 ± 20 mA mg^{-1}_{total} for LCO/NC). This is significantly less than the five-fold increase in total mass activities observed for using nitrogen-doped carbon as compared to the Vulcan carbon supported samples.

To gain more insight into the mechanism of the ORR on LSCO/carbon composite electrodes, the number of electrons transferred was measured through Koutecky-Levich analysis. The Koutecky-Levich plots are shown in **Figure 3** and the full polarization curves are included in Supporting Figures S7 and S8. As expected, the carbons could only perform the first two electron reduction of O_2 to HO_2^-. Although NC was shown to be more active in activation of O_2 through a more positive onset potential, the addition of nitrogen to the carbon did not result in the full 4-electron reduction of O_2 to OH^-. On LCSO, the trends in number of electrons transferred corroborate the activity results, displaying a volcano shape with the middle compositions performing a “pseudo” 4 electron reduction of O_2 to OH^-. Note that the linear fits of the limiting currents for all

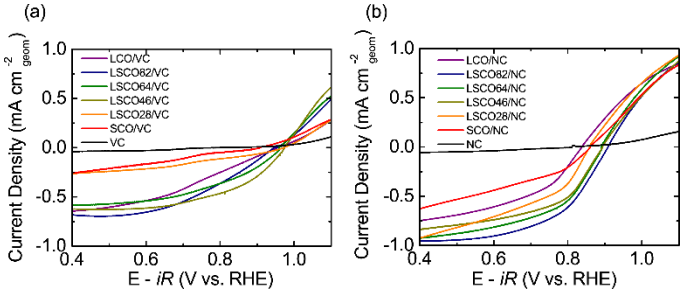

Figure 4. RDE analysis of HPOR/HPRR on LSCO perovskite composite electrocatalysts supported on (**a**) Vulcan carbon and on (**b**) Nitrogen-doped mesoporous carbon at a scan rate of 5 mV s^{-1} and rotation rate of 1600 rpm in 0.1 M KOH with an addition of 1.2 mM H_2O_2. Electrode mass loadings were 35.7 μg cm^{-2}_{geom} for carbon and 15.7 μg cm^{-2}_{geom} for oxide. All polarization curves have been *iR*-corrected.

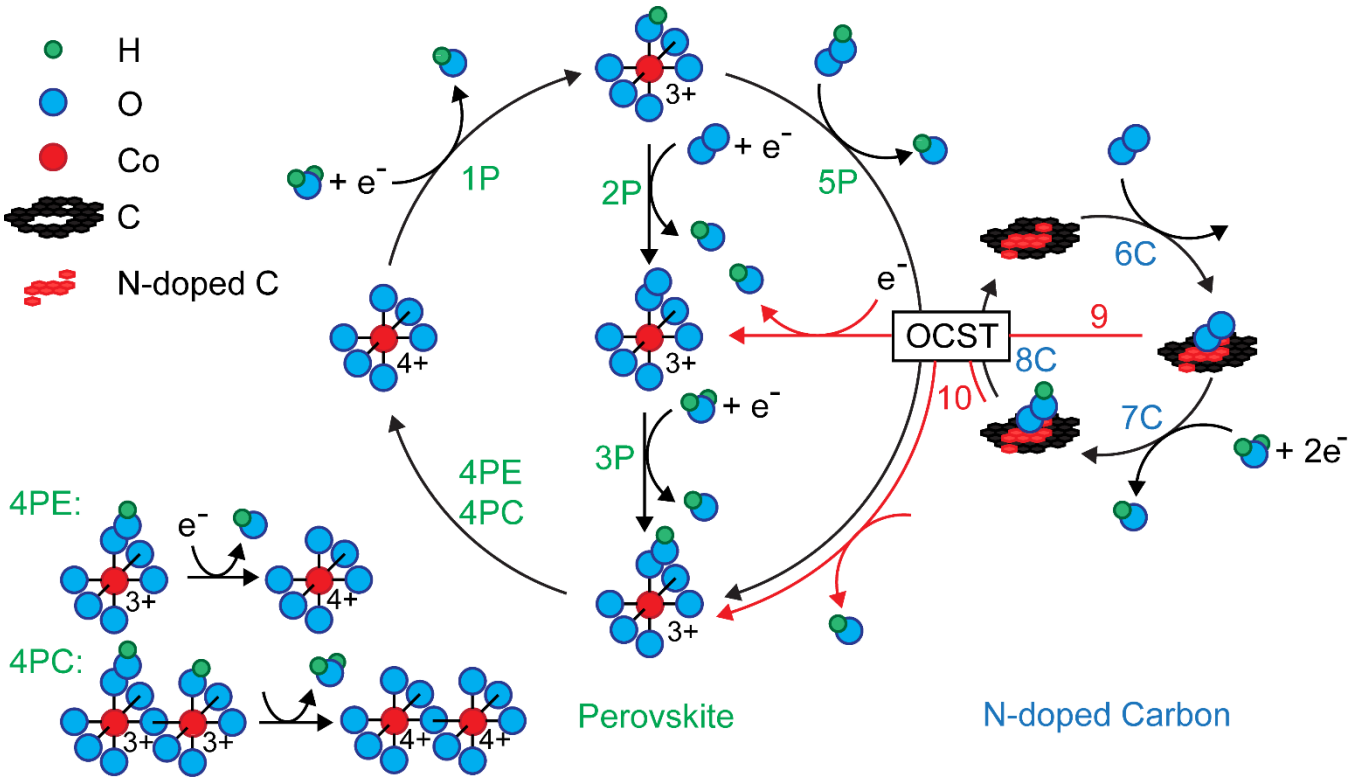

Figure 5. Proposed mechanism of oxygen reduction on LSCO/Carbon composite electrodes. On the LSCO perovskite catalysts (where P refers to a reaction on the perovskite surface) the steps are: (1P) $Co^{3+/4+}$ surface redox step associated with -O and -OH adsorbates; (2P) oxygen adsorption on the Co^{3+} active sites combined with the first electron transfer step; (3P) reduction of the adsorbed oxygen to the HO_2^-; (4PE) electrochemical reduction of the adsorbed HO_2^- to OH^- or (4PC) HO_2^- chemical decomposition; (5P) alternative pathway considering adsorption of HO_2^- on the perovskite surface rather than O_2. On the carbon (where C refers to a reaction on the carbon surface) the hypothesized steps are: (6C) O_2 adsorption; (7C) effective step of O_2 reduction to HO_2^-, note that 6C and 7C yield the overall 2 e^- reduction of O_2 to HO_2^-;(8C) HO_2^- desorption step. Oxygen-containing species transfer steps (OCST) consist of (9) O_2 spillover between the nitrogen-doped carbon active sites and perovskite active sites; (10) HO_2^- spillover between the nitrogen-doped carbon active sites and perovskite active sites. OCST also includes the pathway for the HO_2^- reduction/oxidation on the carbon with (5C) and (8C) steps for both C and N-doped C active sites. Steps (9) and (10); (4PC) and (4PE) were not simulated in parallel, only one of them was introduced to the model simultaneously to check its applicability using the experimental data.

materials investigated in this study do not cross the origin, indicating that the reaction is under mixed kinetic/mass-transfer control even at the limiting potential of 0.4V vs. RHE. In addition, it has been suggested that low numbers of active sites on the catalyst may impose kinetic limitations even in the limiting current regime.[18] Due to the low perovskite weight loading of 30% on carbon as well as the low overall catalyst loading on the electrode (51 µg cm^{-2}_{geom}), this seems like a plausible explanation. The Koutecky-Levich analysis suggests that the adsorption strength of an intermediate produced on the carbon support plays a key role during the reduction of oxygen on LSCO perovskites and that this intermediate is intrinsically linked to the electronic coupling between the perovskite and carbons.

To gain further insight into the ORR reaction mechanism we investigate the reactivity of the hydrogen peroxide reduction (HPRR) and oxidation (HPOR) reactions on the LSCO/carbon composites through rotating-disk electrochemistry, as shown in **Figure 4**. The represented results are the average of triplicate measurements of capacitance averaged forward and backward scans.

The obtained voltammograms generally consist of three electrochemical reactions: (1) HO_2^- reduction to OH^- (HPRR, E_1^0 = 1.74 V vs. RHE @ pH = 13); (2) O_2 reduction to HO_2^- / HO_2^- oxidation to O_2 (HPOR, E_2^0 = 0.74 V vs. RHE @ pH = 13); (3) Full 4e- O_2 reduction to OH^- (ORR, E_3^0 = 1.23 V vs. RHE @ pH = 13). The ORR (reaction (3)) may occur at potentials higher than 0.77 V vs. RHE due to O_2 production by the reverse of reaction (2). Both the VC and NC show negligible activity towards the HPRR, supporting the 2e- ORR pathway on carbons. At the more positive potentials where HPOR may occur, the currents on pure carbons are still much lower than those of the LSCO/carbon composite electrodes. This behavior may be observed only if the reaction (2) is sluggish and has slow rate even at the overpotentials higher than 0.8 V. The mixed current potential (open circuit potential) is shifted towards lower overpotential by ~50 mV for LSCO/NC versus LSCO/VC. The currents on the LSCO/NC composites also tend to increase compared to those

of LSCO/VC. This effect can be explained by the nonequivalent enhancement of the HPOR and HPRR by the NC support leading to the simultaneous increase in currents and shift of the onset potential. While both VC and NC are inactive for HPRR/HPOR, this demonstrates the effect of reaction coupling between the perovskites and the carbon support. In order to better understand this behavior, we deconvolute the contributions of reactions (1) and (2) through the aid of a microkinetic model described below.

Microkinetic Modeling of the ORR/HPOR/HPRR

We consider synergistic mechanistic pathways involving the spillover of oxygen-containing intermediates (either O_2^- or HO_2^-) from the carbon to the oxide in agreement with a number of recent studies on cobalt based perovskites.[16,18,19,27,33,45–51] The reactions are simulated using a microkinetic modeling approach and compared to the experimentally observed catalytic activity trends towards the ORR and HPRR/HPOR for LSCO perovskites and carbons in order to ascertain the dominant pathway.[19,49] Within this framework the proposed reaction mechanisms are used to construct a system of ordinary differential equations, which describes the reaction kinetics together with the mass transport of O_2 and HO_2^- to the vicinity of the electrode. It is solved numerically in the steady-state approximation which can be directly linked with the experiments due to the slow scan rates in the performed experiments. The microkinetic model follows the assumption of Langmuir isotherms for the adsorption/desorption steps and Butler-Volmer electrochemical kinetics for all electron transfer steps. The rate constants for the reaction mechanisms were adjusted until the model qualitatively reproduced experimental findings for ORR RDE and HPRR/HPOR. One can see the full mathematical formulation of the model as well as the parameters adjustment procedure description and their values in the Supporting Information.

Two reaction mechanisms for ORR and HPRR/HPOR on the oxides provided the best explanation for the observed experimental findings. The first one, shown in **Figure 5** adapts the reaction steps proposed by Cushing, Goodenough with (1P), (2P), (3P), (4PE), (5P) steps, where P refers to the reaction occuring on the perovskite surface and PE refers to the electrochemical version of step (4).[12,15,52] The second reaction mechanism, proposed by Strasbourg's group consists of the same reaction steps, but includes an alternative irreversible step of HO_2^- *chemical* decomposition (4PC) instead of (4PE) step.[19,49] It was previously successfully applied to simulate the catalytic activity trends for various oxides in the alkaline media towards the ORR and HPRR/HPOR as well as the kinetic control of HPRR reaction at high overpotentials for the several studied manganese oxides.[53] All the proposed reaction mechanisms were modeled in order to ascertain which mechanism best described the observed trends in the LSCO/VC and NC catalytic activity. The ORR reaction on carbons was simulated by the mechanistic $2e^-$ reduction of O_2 to HO_2^-, which comprises of steps (6C), (7C), and (8C) in Figure 5, where C refers to a step on the carbon surface. It was successfully used previously to describe ORR RDE on carbon without overcomplicating the model.[19,49,53]

According to the XPS data on nitrogen content in the NC, ORR and HPRR/HPOR on NC were modeled through the addition of 2% more active sites, which follow the same reaction mechanism but with faster ORR kinetics.[27] For the NC, the same total active sites surface density was used as for VC because of the following considerations: (i) Catalytic activity of carbons does not linearly scale with the BET or BJH surface areas and (ii) Correct relative rate constants values should be obtained for both NC and VC in order to reproduce the experiment.[20] Hence, the reaction pathway is conserved for both carbons with the renormalization of the reaction rate by the active sites surface density and their contribution to the ORR for the composite materials may be correctly accounted without accurate estimation of their absolute rate constant values.

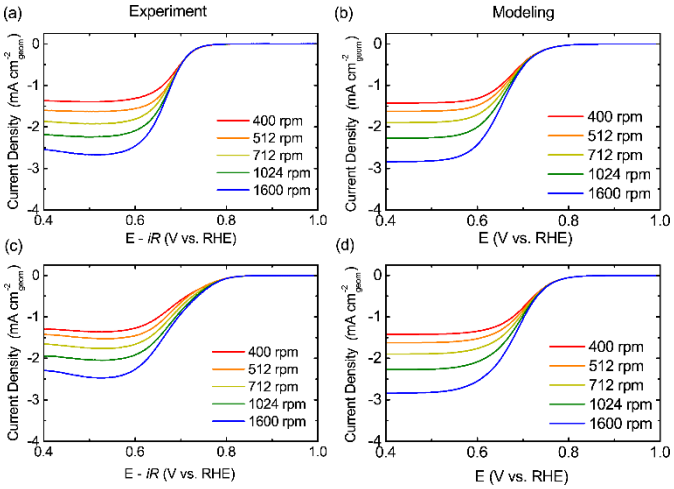

Figure 6. Experimental (**a**, **c**) and simulated (**b**, **d**) ORR RDE voltammograms for Vulcan carbon (**a**, **b**) and nitrogen doped mesoporous carbon (**c**, **d**) in O_2 saturated 0.1 M KOH solution and total electrode mass loadings 35.7 μg cm^{-2}_{geom}.

As the influence of the carbon type on the overall ORR activity is stronger than that of Sr doping ratio on LSCO, the attempt to simulate it is provided first by modeling LCO/VC and LCO/NC using the two abovementioned reaction mechanisms for oxides. Three options of carbon type influence on the overall catalytic activity towards the ORR were considered: 1) Faster ORR kinetics on NC leads to the higher rate of HO_2^- generation, which is further adsorbed and reduced on perovskite, increasing the overall catalytic activity. 2) O_2 spillover between the nitrogen-doped carbon active sites and perovskite active sites in step (9). 3) HO_2^- spillover between the nitrogen-doped carbon active sites and perovskite active sites in step (10). The assumptions 2) and 3) were considered as the spillover of oxygen-containing species was observed experimentally between the carbon and Pt at Pt/C porous electrodes.[54] Hence, an attempt to use the spillover effects could be applied to explain the synergy between the metal oxides and carbon. Effective steps (9) and (10) in Figure 5 serve as an initial attempt

to introduce O_2 and HO_2^- spillover effects to the model. The further refinement of the modeling approach to simulate the spillover effects requires additional experimental data to better understand the oxide/carbon interface.

The consecutive way in which the model parameters are adjusted are as follows: 1) The VC and NC rate constants were adjusted to reproduce the experimental ORR and HPRR/HPOR results on the respective bare carbons; 2) Using the adjusted VC rate constants, the LCO rate constants were adjusted to reproduce experimental data for ORR and HPRR/HPOR at LCO/VC within the reaction mechanisms with (4PC) and (4PE) steps; 3) Using the previously adjusted parameters for LCO and NC, the abovementioned hypotheses for carbon type influence were tested; and 4) The most successful reaction mechanism and hypothesis for the carbon type influence were applied to describe the catalytic activity trends with the Sr doping ratio in LSCO. For these reasons, the modeling parameters are provided for the most active composition, LSCO64.

to that of VC was reproduced. The more detailed simulation of the well-observed minimum of ORR currents at 0.55 V vs. RHE for NC, as well as the voltammograms shape at average potentials, require the improvement of the model, with possible addition of a 4 e^- O_2 to OH^- oxygen reduction pathway occuring on the carbon (rather than the 2 e^- O_2 to HO_2^-) with competition of different active sites at NC at low overpotentials and carbon surface poisoning at high overpotentials.[55] In order to do that, additional experimental studies are required to make the model improvement physically relevant. The negligible simulated HPOR/HPRR currents on the VC and NC are consistent with the low values observed in experiments.

The results of the LCO/VC simulation are shown in **Figure 7**. Both models, using either the (4PE) or the (4PC) step for HO_2^- decomposition, semi-quantitatively reproduce ORR RDE voltammograms. Within the model considering the (4PC) step the ORR proceeds on the LCO/VC composite material through steps (6C), (7C), (8C), (5P), (4PC), 2 x (1P). The LCO by itself has

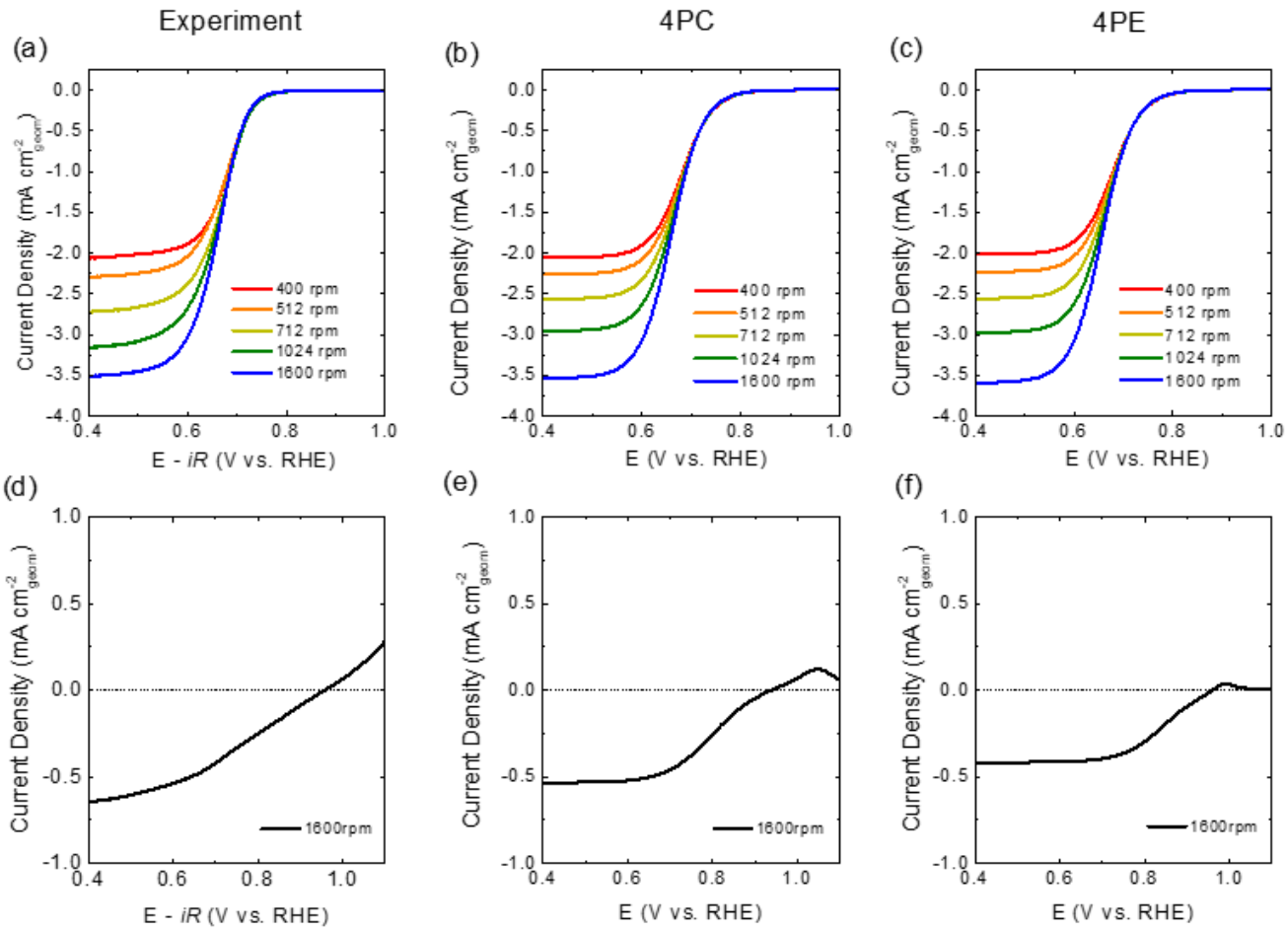

Figure 7. ORR RDE voltammograms (**a**-**c**) in O_2 saturated 0.1 M KOH. HPRR/HPOR RDE voltammograms (**d**-**f**) in Ar-purged 0.1 M KOH solution with 1.2 mM HO_2^-. 30 wt% LCO/VC composite catalyst was used with total electrode mass loading equal to 51 μg cm^{-2}_{geom}. (**a**, **d**) – experimental results. (**b**, **e**) – modeling results with the (4PC) reaction mechanism. (**c**, **f**) – modeling results with the 4PC reaction mechanism.

The simulated ORR RDE voltammograms for the carbons, shown in **Figure 6**, qualitatively reproduce experimental results. For the NC, the positive shift of ORR onset potential comparing

a slow (2P) step which prohibits the consecutive 2e^- + 2e^- pathway on the oxide. The model qualitatively reproduces the zero current potential as well as the incipient current regions

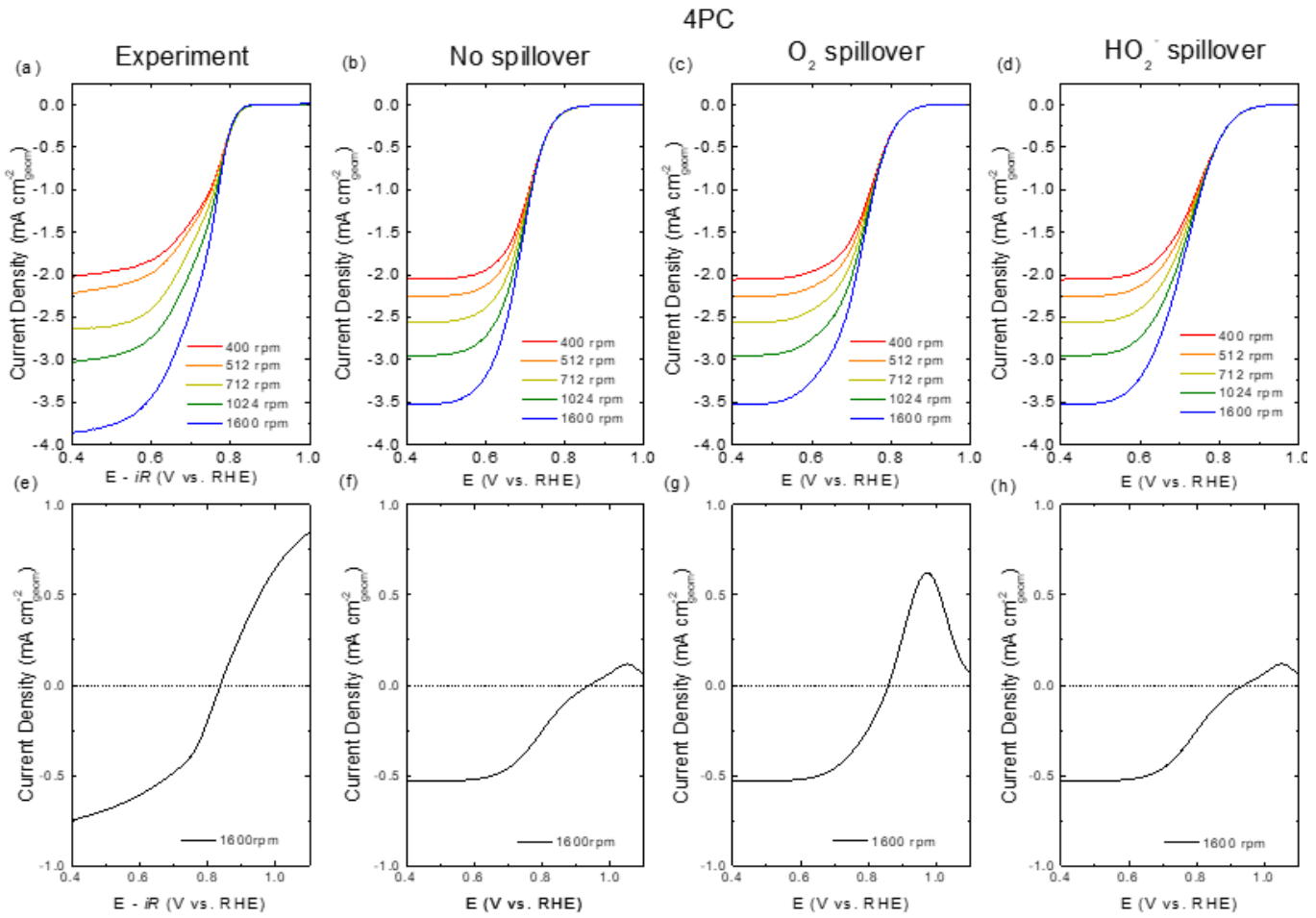

Figure 8. ORR RDE voltammograms (a-d) in O_2 saturated 0.1 M KOH. HPRR/HPOR RDE voltammograms (e-h) in Ar-purged 0.1 M KOH solution with 1.2mM HO_2^-. 30 wt% LCO/NC composite catalyst was used with total electrode mass loading equal to 51 μg cm^{-2}_{geom}. (a, e) – experimental results. (b, f), (c, g), (d, h) – modeling results for (4PC) reaction mechanism without/with O_2/with HO_2^- spillover respectively.

for HPRR/HPOR RDE voltammograms. The reaction mechanism following the (4PC) step shows better results for the reproduction of HPRR kinetically limiting currents at high overpotentials due to the higher degree of freedom for the simultaneous adjustment of ORR and HPRR kinetically-limiting currents with the two chemical steps (4PC) and (5P). Both models have limitations on the maximum positive potential that can be applied because the surface active sites are passivated at the positive potentials by the reverse reaction (-1P). One can potentially overcome this limitation via the introduction of interactions between the adsorbed reaction intermediates via Frumkin isotherms, consideration of the outersphere reaction regime at positive potentials, or inclusion of multiple LCO active sites with different distributions of their formal surface redox potential. All of these require additional experimental data beyond the scope of this study. Similar results on LCO/NC (Figure S11) shows that neither increased ORR activity of NC towards the $2e^-$ oxygen reduction, nor HO_2^- and O_2 spillover steps can explain simultaneous increase in HPOR currents, ORR currents, and change of the ORR currents slope at the LCO/NC within the model assumptions and (4PE) step for HO_2^- reduction. The rate constants for spillover steps were adjusted to reproduce the shift in the ORR onset potential. Additionally, an artificial minimum of ORR currents was observed with the O_2 and HO_2^- spillover due to the competitive O_2 reduction at the VC and NC active sites. Thus we exclude the 4PE pathway in the mechanism of the ORR on the LSCO/carbon composites.

For the nitrogen-doped carbon (NC) the best result of simultaneous qualitative reproduction of experimental results was obtained for the reaction mechanism with the (4PC) step for HO_2^- decomposition and (9) O_2 spillover step, as shown in **Figure 8**. This option was able to reproduce: (i) The negative shift of the HPRR/HPOR mixed current potential, (ii) The initial HPOR region, (iii) The positive onset potential shift for the ORR, (iv) slope change of the ORR RDE voltammograms. However, the increased HPRR currents at high overpotentials are not well reproduced. Both VC and NC carbons show no activity towards the HPRR, and the HPRR limiting currents are described by the rate of (4PC) reaction. The HPOR current was increased because the backward O_2 spillover step (-9) overcame the reaction limiting step of HO_2^- adsorption on carbon (-8C) and slow oxygen desorption from the LCO (-2P). The increased activity for

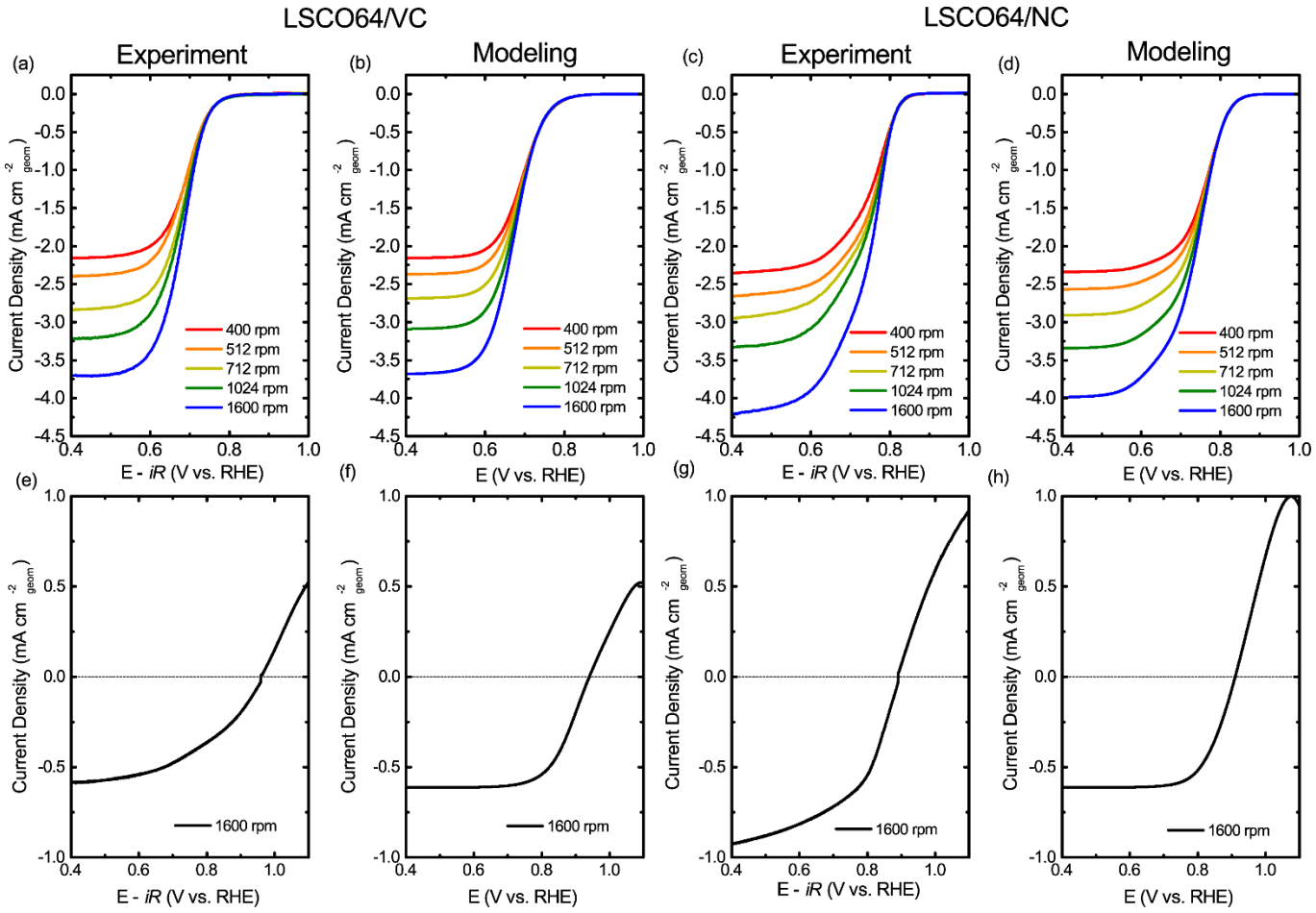

Figure 9. ORR RDE voltammograms (a-d) in O_2 saturated 0.1 M KOH. HPRR/HPOR RDE voltammograms (e-h) in Ar-purged 0.1 M KOH solution with 1.2mM HO_2^-. 30 wt% LCO/NC composite catalyst was used with total electrode mass loading equal to 51 μg cm^{-2}_{geom}. (a, e), (c, g) – experimental results for LSCO/VC and LSCO64/NC respectively. (b, f), (d, h) – modeling results using the reaction mechanism with (4PC) step for LSCO/VC and LSCO64/NC respectively.

ORR and a positive shift of the ORR onset potential is attributed to a change in the RLS from O_2 → O_2^- on VC to O_2^- → HO_2^- on NC which increased the relative amount of O_2^- relative to HO_2^- resulting in O_2 spillover (9) rather than hydroperoxide (10). The O_2 spillover is considered as a charge transfer event and differs from step (2P) in that the NC is considered to be the active site for charge transfer (leading to differing rate constants k_9/k_{-9}). Note that the O_2 spillover step (9) was also considered for LCO/VC (Figure S12) but was not able to reproduce the HPRR/HPOR experimental results suggesting that the incorporation of nitrogen alters the mechanism of the composite electrodes. The slope change refers to the shift from the reaction regime at lower overpotentials where N-doped active sites participate in the reaction together with O_2 spillover, and the reaction regime with HO_2^- generation (6C), (7C) on the carbon, its desorption (8C) and re-adsorption (5P) on perovskite at larger overpotentials, where the N-doped active sites contribution is lower due to the competitive $2e^-$ oxygen reduction on carbon and N-doped active sites. The other options such as higher NC activity (Figure 9, (2a), (2b)) and HO_2^- spillover (Figure 4, (2a), (2b)) are not able to simultaneously reproduce ORR and HPRR/HPOR RDE voltammograms. This suggests a differing mechanism in the oxygen-containing species transfer step (9) or (10) when nitrogen is introduced into the carbon structure and may indicate the buildup of a superoxide like O_2^- on nitrogen-doped carbon causing superoxide spillover (9) rather than hydroperoxide (10).

Finally, an attempt to model the higher catalytic activity of LSCO64 was made as shown in **Figure 9**. The higher surface hydroxylation at higher Sr content was qualitatively modeled by positively shifting the surface Co^{3+}/Co^{4+} formal redox potential by 120 mV relative to LCO. If one wants to fix this parameter as it was done for LCO, the same experimental procedure should be applied.[18] The transfer coefficient for the (2P) step was changed from the 0.5 to 0.8 to reproduce the ORR RDE voltammograms slopes. The forward and backward rate constants should be unavoidably simultaneously adjusted for (2P) (increased 2 times), (3P) (decreased 10 times), and (9) (increased 2 times) reaction steps. For the LSCO64 the ORR kinetically limiting currents at high overpotentials are different for VC and NC support, which is opposite to what was observed at LCO. From the modeling point of view, it could be explained by (i) the faster (4PC) step, or different influence of the carbon type on the oxide utilization via the improvement of the

electrical contact. In order to check it, an oxide utilization enhancement should be experimentally estimated.[18] Moreover, because the LSCO64 has lower bulk stability than LCO, one cannot exclude an option that the surface structure, as well as the surface active sites and their density, are different from the ones for LCO.[25] Regardless, the modeling suggests that the origin in the higher catalytic activity originates from a fast peroxide decomposition (4PC) step.

On LCO/VC,NC and LSCO64/VC,NC the rate-limiting step was identified as the decomposition of the hydroperoxide adsorbate (4PC). This step requires both OH^- and HO_2^- adsorbates and results in a Co^{4+} species. Considering the XPS hydroxylation information and the oxidation state data derived through iodometric titrations, the high reactivity of LSCO46 and LSCO64 can be explained as an optimal balance in both intermediate oxidation state (which reflects the energy of the electronic states of the catalyst) and relative hydroxylation. In contrast, SCO, which has a similar oxidation state but higher surface hydroxylation results in low HPOR/HPRR/ORR activity. Similarly, LCO has a lower oxidation state and lower surface hydroxylation resulting in low activity. The change in Tafel slope at high potentials for NC (in comparison to VC) can be explained by a higher mass transfer of reactants through the O_2 spillover step (9) leading to high coverage of intermediates at lower overpotential.

Conclusions

In summary, the oxidation state of cobalt and surface hydroxylation (vacancy concentration) were modulated through Sr substitution to investigate the activity for $La_{1-x}Sr_xCoO_{3-\delta}$ perovskites/carbon composite electrodes for the ORR. In addition, the role of carbon as a co-catalyst was investigated through supporting the LSCO catalysts on either Vulcan carbon with no nitrogen or on a 2 at. % N-doped carbon. It was found that the interactions between LSCO and carbon in composite systems played a crucial role in describing the activity of the series. The proposed microkinetic model qualitatively reproduced experimental data for ORR RDE on VC and NC, ORR and HPRR/HPOR data for LCO/VC, NC, and LSCO64/VC, NC. Within the assumptions of the developed model, two reaction mechanisms with chemical and electrochemical hydroperoxide decomposition steps were considered. Three hypotheses for the catalytic activity enhancement due to nitrogen incorporation in the carbon were elucidated. It was shown that the reaction mechanism with a chemical step for HO_2^- decomposition on the perovskite surface, HO_2^- mass transfer between VC and and the perovskite, and O_2 spillover between the NC and perovskite active sites provided the best qualitative reproduction for the ORR and HPRR/HPOR RDE experiments. Despite the simplified model for ORR and HPOR/HPRR on carbon and neglection of adsorbates interactions, the results of this work show that use of a nitrogen-doped carbon support leads to a 5-fold catalytic activity enhancement for ORR on LSCO/carbon composites through enhancement of the O_2 spillover pathway. This work serves as the first step to the elucidation of carbon support influence in composite oxide/carbon electrodes and a better description of catalytic activity trends with Sr doping ratio in LSCO. From this study, it is clear that the rational design of perovskite electrocatalysts requires a complete understanding of the composite systems used in the studies and that the role of carbon in the reduction of oxygen on metal oxides cannot be overlooked.

Methods

All chemicals were used as received. Anhydrous ethanol and 5 wt% Nafion solution in lower alcohols were purchased from Sigma-Aldrich. Lanthanum (III) nitrate hexahydrate (99.999%), strontium (II) nitrate hexahydrate (99.9%), cobalt (II) nitrate hexahydrate (99.9%), tetrapropylammonium bromide (98%), tetramethylammonium hydroxide pentahydrate (99%), 2-propanol, and potassium hydroxide were obtained from Fisher Scientific. Absolute ethanol (200 proof) was obtained from Aaper alcohol. Oxygen (99.999%) gas was obtained from Praxair. Vulcan carbon XC-72 (VC) was obtained from Cabot Corporation, and the nitrogen-doped carbon (NC) was prepared as reported elsewhere.[56] The LSCO series was synthesized according to the methods described in our previous papers.[25–28]

X-ray Photoelectron Spectroscopy:

O1s X-ray photoelectron spectroscopy of the LSCO series was collected using a Kratos AXIS Ultra DLD Photoelectron Spectrometer calibrated against the Ag 3*d* spectrum of freshly sputtered 99.99% pure Ag. Due to the semiconducting properties of the LSCO member, charge neutralization was employed in order to collect high resolution data. Binding energy shifts due to charging were compensated by reconstruction of the La $3d_{5/2}$ spectra, as outlined by Mickevicius *et al.*[57] Full details regarding the deconvolution of the LSCO O1s spectra can be found in the Supporting Information.

Electron Microscopy:

The TEM samples were prepared by crushing the crystals in a mortar in ethanol and depositing drops of suspension onto holey carbon grid. TEM images, high angle annular dark field scanning transmission electron microscopy (HAADF-STEM) images, annular bright field STEM (ABF-STEM) images and energy dispersive X-ray (EDX) spectra were obtained with an aberration-corrected Titan G^3 electron microscope operated at 200 kV using a convergence semi-angle of 21.6 mrad. The HAADF and ABF inner collection semi-angles were 70 mrad and 10 mrad, respectively.

Electrode preparation:

All $La_{1-x}Sr_xCoO_{3-\delta}$ nanopowders were loaded onto carbon through ball milling with a Wig-L-Bug ball mill. For rotating disk electrode (RDE) and for the rotating ding-disk electrode (RRDE) measurements the LSCO nanopowders were loaded at a mass loading of ~30 wt% onto either VC (BET Surface Area = 235 m^2 g^{-1}; Supporting Information Figure S13) or NC (BET Surface Area = 1080 m^2 g^{-1}).[27] SEM of the composites can be found in the Supporting Information Figures S6 and S7. LSCO/carbon

mixtures were dispersed in ethanol containing 0.05 wt% Na-substituted Nafion at a ratio of 1 mg mL^{-1} and sonicated for 45 min. This solution was spuncast onto a glassy carbon rotating disk electrode (0.196 cm^2, Pine Instruments) and for the rotating ring-disk electrode (Glassy Carbon Disk: 0.2472 cm^2_{geom}; Pt ring: 0.1859 cm^2, Pine Instruments) at a total mass loading of 51.0 μg cm^{-2}_{geom} (LSCO loading: 15.3 μg cm^{-2}_{geom}). The electrodes were cleaned prior to spincasting by sonication in a 1:1 de-ionized water:ethanol solution. The electrodes were then polished using 50 nm alumina powder, sonicated in a fresh deionized water:ethanol solution, and dried under a scintillation vial in ambient air.

Electrochemical Testing:

Electrochemical testing was performed on a CH Instruments CHI832a potentiostat or a Metrohm Autolab PGSTAT302N potentiostat, both equipped with high speed rotators from Pine Instruments. Both RDE and RRDE ORR tests were performed at room temperature in O_2 saturated 0.1 M KOH (measured pH ≈ 12.6). The current interrupt and positive feedback methods were used to determine electrolyte resistance (50 Ω) and all data was *iR* compensated after testing. Each measurement was performed in a standard three-electrode cell using a Hg/HgO (1 M KOH) reference electrode, a Pt wire counter electrode, and a film of catalyst ink on the glassy carbon working electrode. All ORR testing was performed on a new electrode that had not undergone previous testing. The mass-normalized kinetic current densities Tafel plots were generated after applying the mass-transport correction derived from the Levich equation, where i_k represents the kinetic current density, i_L is the mass-transport limited current density at 0.4V vs. RHE, and i is the current density at a given potential:

$$i_k = i_L(i)(i_L - i)^{-1} \quad (1)$$

Tafel plots represent the average mass-transport corrected currents at a given potential for the 5 electrodes used in the Koutecky-Levich analysis. For the Koutecky-Levich analysis, cyclic voltammetry was performed from +1.0 to +0.4 V at 5 mV s^{-1} at rotation rates of ω = 400, 522, 712, 1024, and 1600 rpm. The number of electrons were determined through the slope of i_L^{-1} vs. $\omega^{-1/2}$ according to the Koutecky-Levich equation:[58]

$$i^{-1} = i_k^{-1} + i_L^{-1} \quad (2)$$

$$i_L = 0.62nFAC_{O2}D_{O2}^{2/3}v^{-1/6}\omega^{1/2} \quad (3)$$

Where n is the number of electrons transferred during the reaction, F is Faraday's constant, A is the geometric area of the electrode, C_{O2} is the concentration of oxygen at saturation levels in 0.1 M KOH, D_{O2} is the diffusion coefficient of oxygen in 0.1 M KOH, v is the kinematic viscosity of 0.1 M KOH, and ω is the rotation rate of the electrode in rad/s.[59] The current at +0.693V was selected from the polarization curves to compare the composite mass activities. For the peroxide studies, the same methodology was used with an electrolyte consisting of 1.2 mM H_2O_2 in Ar-saturated 0.1 M KOH. Cyclic voltammetry was performed by scanning either +/- 500 mV from the measured open circuit potential at a scan rate of 5 mV s^{-1} and an electrode rotation rate of 1600 rpm. The measurements were carried out in triplicate using a freshly prepared electrode for each measurement. Electrodes subjected to scans in the anodic potential direction from OCV were not tested in the cathodic and vice versa. The data presented is an average of the triplicate measurements. All potentials are reported versus the reversible hydrogen electrode (RHE), which was measured as $E_{RHE} = E_{Hg/HgO}$ + 0.8456 V through the reduction of hydrogen in 1 atm H_2 saturated 0.1 M KOH.

Conflicts of interest

There are no conflicts to declare.

Acknowledgements

Financial support for this work was provided by the R. A. Welch Foundation (grants F-1529 and F-1319). S.D. was supported as part of the Fluid Interface Reactions, Structures and Transport (FIRST) Center, an Energy Frontier Research Center funded by the U.S. Department of Energy, Office of Science, and Office of Basic Energy Sciences.

Notes and references

1 Y. Gorlin and T. F. Jaramillo, *J. Am. Chem. Soc.*, 2010, **132**, 13612–13614.
2 V. Neburchilov, H. Wang, J. J. Martin and W. Qu, *Journal of Power Sources*, 2010, **195**, 1271–1291.
3 F. Bidault, D. J. L. Brett, P. H. Middleton and N. P. Brandon, *Journal of Power Sources*, 2009, **187**, 39–48.
4 F. Cheng and J. Chen, *Chem. Soc. Rev.*, 2012, **41**, 2172–2192.
5 Y. Lee, J. Suntivich, K. J. May, E. E. Perry and Y. Shao-horn, *Journal of Physical Chemistry Letters*, 2012, **3**, 399–404.
6 X. Huang, Z. Zhao, L. Cao, Y. Chen, E. Zhu, Z. Lin, M. Li, A. Yan, A. Zettl, Y. M. Wang, X. Duan, T. Mueller and Y. Huang, *Science*, 2015, **348**, 1230–1234.
7 F. H. B. Lima, J. Zhang, M. H. Shao, K. Sasaki, M. B. Vukmirovic, E. A. Ticianelli and R. R. Adzic, *J. Phys. Chem. C*, 2007, **111**, 404–410.
8 D. B. Meadowcroft, *Nature*, 1970, **226**, 847–848.
9 M. a Peña and J. L. Fierro, *Chemical reviews*, 2001, **101**, 1981–2017.
10 C. K. Lee, K. A. Striebel, F. R. McLarnon and E. J. Cairns, *J. Electrochem. Soc.*, 1997, **144**, 3801–3806.
11 A. Weidenkaff, S. G. Ebbinghaus and T. Lippert, *Chem. Mater.*, 2002, **14**, 1797–1805.
12 J. Suntivich, H. A. Gasteiger, N. Yabuuchi, H. Nakanishi, J. B. Goodenough and Y. Shao-Horn, *Nat Chem*, 2011, **3**, 546–550.
13 K. Kinoshita, *Carbon: Electrochemical and Physiochemical Properties*, John Wiley & Sons, New York, 1998.
14 Z. Zhang, J. Liu, J. Gu, L. Su and L. Cheng, *Energy Environ. Sci.*, 2014, **7**, 2535–2558.
15 Z.-L. Wang, D. Xu, J.-J. Xu and X.-B. Zhang, *Chem. Soc. Rev.*, 2014, **43**, 7746–7786.
16 E. Fabbri, R. Mohamed, P. Levecque, O. Conrad, R. Kötz and T. J. Schmidt, *ACS Catal.*, 2014, **4**, 1061–1070.

17 R. Mohamed, X. Cheng, E. Fabbri, P. Levecque, R. Kötz, O. Conrad and T. J. Schmidt, *J. Electrochem. Soc.*, 2015, **162**, F579–F586.
18 T. Poux, F. S. Napolskiy, T. Dintzer, G. Kéranguéven, S. Y. Istomin, G. A. Tsirlina, E. V. Antipov and E. R. Savinova, *Catalysis Today*, 2012, **189**, 83–92.
19 T. Poux, A. Bonnefont, G. Kéranguéven, G. A. Tsirlina and E. R. Savinova, *ChemPhysChem*, 2014, **15**, 2108–2120.
20 A. S. Ryabova, A. Bonnefont, P. A. Simonov, T. Dintzer, C. Ulhaq-Bouillet, Y. G. Bogdanova, G. A. Tsirlina and E. R. Savinova, *Electrochimica Acta*, 2017, **246**, 643–653.
21 K. Miyazaki, K. Kawakita, T. Abe, T. Fukutsuka, K. Kojima and Z. Ogumi, *J. Mater. Chem.*, 2011, **21**, 1913–1917.
22 S. Zhao, L. Yan, H. Luo, W. Mustain and H. Xu, *Nano Energy*, 2018, **47**, 172–198.
23 M. Chen, L. Wang, H. Yang, S. Zhao, H. Xu and G. Wu, *Journal of Power Sources*, 2018, **375**, 277–290.
24 C. T. Alexander, A. M. Abakumov, R. P. Forslund, K. P. Johnston and K. J. Stevenson, *ACS Appl. Energy Mater.*, 2018, **1**, 1549–1558.
25 J. T. Mefford, X. Rong, A. M. Abakumov, W. G. Hardin, S. Dai, A. M. Kolpak, K. P. Johnston and K. J. Stevenson, *Nat Commun*, 2016, **7**, 11053.
26 W. G. Hardin, D. a. Slanac, X. Wang, S. Dai, K. P. Johnston and K. J. Stevenson, *The Journal of Physical Chemistry Letters*, 2013, **4**, 1254–1259.
27 W. G. Hardin, J. T. Mefford, D. A. Slanac, B. B. Patel, X. Wang, S. Dai, X. Zhao, R. S. Ruoff, K. P. Johnston and K. J. Stevenson, *Chem. Mater.*, 2014, **26**, 3368–3376.
28 J. T. Mefford, W. G. Hardin, S. Dai, K. P. Johnston and K. J. Stevenson, *Nat Mater*, 2014, **13**, 726–732.
29 J. O. Bockris and T. Otagawa, *J. Phys. Chem.*, 1983, **87**, 2960–2971.
30 J. O. Bockris and T. Otagawa, *J. Electrochem. Soc.*, 1984, **131**, 290–302.
31 Y. Matsumoto, H. Yoneyama and H. Tamura, *Journal of Electroanalytical Chemistry and Interfacial Electrochemistry*, 1977, **83**, 237–243.
32 Y. Matsumoto, H. Yoneyama and H. Tamura, *Bulletin of the Chemical Society of Japan*, 1978, **51**, 1927–1930.
33 X. Li, W. Qu, J. Zhang and H. Wang, *J. Electrochem. Soc.*, 2011, **158**, A597–A604.
34 H. Kim, K. Lee, S. I. Woo and Y. Jung, *Phys. Chem. Chem. Phys.*, 2011, **13**, 17505–17510.
35 Z. Luo, S. Lim, Z. Tian, J. Shang, L. Lai, B. MacDonald, C. Fu, Z. Shen, T. Yu and J. Lin, *Journal of Materials Chemistry*, 2011, **21**, 8038.
36 J. D. Wiggins-Camacho and K. J. Stevenson, *J. Phys. Chem. C*, 2009, **113**, 19082–19090.
37 J. D. Wiggins-Camacho and K. J. Stevenson, *J. Phys. Chem. C*, 2011, **115**, 20002–20010.
38 Y. Matsumoto and E. Sato, *Electrochimica Acta*, 1979, **24**, 421–423.
39 Y. Matsumoto, H. Yoneyama and H. Tamura, *Journal of Electroanalytical Chemistry and Interfacial Electrochemistry*, 1977, **79**, 319–326.
40 Y. Matsumoto, J. Kurimoto and E. Sato, *Journal of Electroanalytical Chemistry and Interfacial Electrochemistry*, 1979, **102**, 77–83.
41 Y. Matsumoto and E. Sato, *Materials Chemistry and Physics*, 1986, **14**, 397–426.
42 E. Fabbri, M. Nachtegaal, X. Cheng and T. J. Schmidt, *Advanced Energy Materials*, **5**, 1402033.
43 Y. Liang, Y. Li, H. Wang, J. Zhou, J. Wang, T. Regier and H. Dai, *Nat Mater*, 2011, **10**, 780–786.
44 Y. Liang, H. Wang, J. Zhou, Y. Li, J. Wang, T. Regier and H. Dai, *J. Am. Chem. Soc.*, 2012, **134**, 3517–3523.
45 V. Hermann, D. Dutriat, S. Müller and C. Comninellis, *Electrochimica Acta*, 2000, **46**, 365–372.
46 G. Kéranguéven, S. Royer and E. Savinova, *Electrochemistry Communications*, 2015, **50**, 28–31.
47 S. Malkhandi, B. Yang, a. K. Manohar, a. Manivannan, G. K. S. Prakash and S. R. Narayanan, *The Journal of Physical Chemistry Letters*, 2012, **3**, 967–972.
48 S. Malkhandi, P. Trinh, A. K. Manohar, K. C. Jayachandrababu, A. Kindler, G. K. S. Prakash and S. R. Narayanan, *J. Electrochem. Soc.*, 2013, **160**, F943–F952.
49 T. Poux, A. Bonnefont, A. Ryabova, G. Kéranguéven, G. A. Tsirlina and E. R. Savinova, *Phys. Chem. Chem. Phys.*, 2014, **16**, 13595–13600.
50 Y. Shimizu, K. Uemura, H. Matsuda, N. Miura and N. Yamazoe, *J. Electrochem. Soc.*, 1990, **137**, 3430–3433.
51 J. Sunarso, A. a. J. Torriero, W. Zhou, P. C. Howlett and M. Forsyth, *The Journal of Physical Chemistry C*, 2012, **116**, 5827–5834.
52 Y. Wang and H.-P. Cheng, *J. Phys. Chem. C*, 2013, **117**, 2106–2112.
53 A. S. Ryabova, A. Bonnefont, P. Zagrebin, T. Poux, R. Paria Sena, J. Hadermann, A. M. Abakumov, G. Kéranguéven, S. Y. Istomin, E. V. Antipov, G. A. Tsirlina and E. R. Savinova, *ChemElectroChem*, 2016, **3**, 1667–1677.
54 W. C. Conner and J. L. Falconer, *Chem. Rev.*, 1995, **95**, 759–788.
55 I. Morcos and E. Yeager, *Electrochimica Acta*, 1970, **15**, 953–975.
56 X. Wang, J. S. Lee, Q. Zhu, J. Liu, Y. Wang and S. Dai, *Chem. Mater.*, 2010, **22**, 2178–2180.
57 S. Mickevičius, S. Grebinskij, V. Bondarenka, B. Vengalis, K. Šliužienė, B. A. Orlowski, V. Osinniy and W. Drube, *Journal of Alloys and Compounds*, 2006, **423**, 107–111.
58 A. J. Bard and L. R. Faulkner, *Electrochemical Methods: Fundamentals and Applications*, John Wiley & Sons, Inc., New York, 2nd edn., 2001.
59 H. A. Gasteiger and P. N. Ross, *J. Phys. Chem.*, 1996, **100**, 6715–6721.

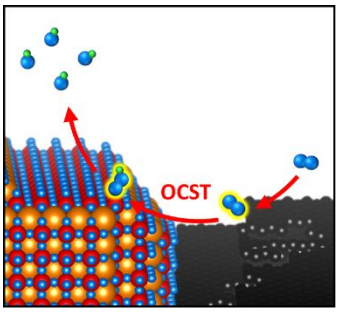

Experiment and microkinetic modeling decouple the synergistic roles of $La_{1-x}Sr_xCoO_{3-\delta}$ perovskite oxides and carbon additives during the oxygen reduction reaction.